POST IMPACT COMPRESSIVE BEHAVIOR OF COMPOSITES

Kuen Y. Lin* and Rufeng Li †

Department of Aeronautics and Astronautics
University of Washington
Seattle, Washington 98195, U.S.A.

Abstract

In this paper, the post impact compressive behavior of polymeric composites is studied both analytically and experimentally. In the analytical study, a closed-form solution is obtained for postbuckling of composites with a circular delamination. Using this solution, the reduced stiffness of the impact damaged region is calculated and the residual compressive strengths of quasi-isotropic laminates are predicted as a function of damage size. In the experimental study, in-plane displacements near the damaged region are determined by employing a micro moire interferometry technique. The strain concentrations as well as the compression-after-impact strength have been measured and compared with analytical predictions. Good agreement between the predicted results and experimental data was observed.

Introduction

An important issue in applying polymeric composites to primary aircraft structures is the impact damage tolerance. Typically a laminated composite absorbs impact energy via fiber fracture, matrix cracking, and interface delamination. The type and amount of damage induced by impact generally depend upon specific material system used, layup orientation, as well as the impactor geometry. When these material and structural factors are kept constant, the impact damage can be well characterized using a nondestructive technique such as C-scanning. With the damage state defined, the problem reduces to the determination of residual strength of composites after impact, particular the compressive strength. After that, guidelines for inspecting composite structures containing impact damage can be developed.

In this paper, the post impact compressive behavior of polymeric composites is studied both analytically and experimentally. In the analytical study, a closed-form solution based on von Karman's nonlinear strain displacement relations is obtained for postbuckling of composites containing circular delaminations. Using the developed solution, the reduced stiffness of the damaged region is calculated. The compression-after-impact (CAI) strength of composite is then predicted using the method proposed by Dost, Ilcewicz, and Gosse (DIG) in [1]. In the experimental study, in-plane displacements on the impacted side are measured using a micro moire interferometry technique. The out-of-plane displacement on the opposite side is measured using the shadow moire method. The strain concentrations near the damaged region as well as the CAI strength are then determined. The predicted results are then compared with the experimental data.

Postbuckling Solutions

In certain laminates subjected to impact, such as a quasi-isotropic layup, a representative damage pattern exists in the form of a sublaminate. This sublaminate often buckles under a compressive load which can trigger compressive failures. Thus, the stability and post buckling behavior is important in order to develop a method for predicting the CAI strength. The critical buckling load for a circular sublaminate was analyzed in [2] using a simple quadratic polynomial. In the following, a more general approach is developed for analyzing buckling and postbuckling behavior of a sublaminate. This analysis procedure is based on the Rayleigh-Ritz method for geometric nonlinear problems. The three-dimensional displacements of a circular sublaminate are expressed in a finite series so that convergence of the numerical solution can be properly studied.

Consider a circular delamination as shown in Figure 1. Using von Karman's non-linear strain-displacement relation, we have

$$\{\varepsilon\} = \{\varepsilon_0\} + \{\chi\} + \{\varepsilon_n\} \tag{1}$$

where

$$\{\varepsilon_0\} = \left[\frac{\partial u}{\partial r}, \frac{1}{r}\frac{\partial v}{\partial \theta} + \frac{u}{r}, \frac{1}{r}\frac{\partial u}{\partial \theta} + \frac{\partial v}{\partial r} - \frac{v}{r}\right]^T$$

$$\{\chi\} = \left[-\frac{\partial^2 w}{\partial r^2}, -\frac{1}{r^2}\frac{\partial^2 w}{\partial \theta^2}, -\frac{2}{r}\frac{\partial^2 w}{\partial r \partial \theta} + \frac{2}{r^2}\frac{\partial w}{\partial \theta}\right]^T$$

$$\{\varepsilon_n\} = \left[\frac{1}{2}\left(\frac{\partial w}{\partial r}\right)^2, \frac{1}{2r^2}\left(\frac{\partial w}{\partial \theta}\right)^2, \frac{1}{r}\frac{\partial w}{\partial r}\frac{\partial w}{\partial \theta}\right]^T \tag{2}$$

* Professor, † Graduate Research Assisstant.

Based on Kirchhoff's plate theory, the potential energy of the composite laminate subjected to applied strain $\bar{\varepsilon}_x$ is

$$\Pi = U_L + U_{NL} - V \tag{3}$$

where

$$U_L = \frac{1}{2}\iint_S \left(\{\varepsilon_0\}^T[A]\{\varepsilon_0\} + \{\varepsilon_0\}^T[B]\{\chi\} + \{\chi\}^T[B]\{\varepsilon_0\} + \{\chi\}^T[D]\{\chi\}\right)dS \tag{4}$$

$$U_{NL} = \frac{1}{2}\iint_S \left(\{\varepsilon_0\}^T[A]\{\varepsilon_n\} + \{\varepsilon_n\}^T[A]\{\varepsilon_0\} + \{\varepsilon_n\}^T[A]\{\varepsilon_n\} + \{\varepsilon_n\}^T[B]\{\chi\} + \{\chi\}^T[B]\{\varepsilon_n\}\right)dS \tag{5}$$

$$V = \iint_S \{P_0\}^T\{\varepsilon_n\}dS = \frac{1}{2}\iint_S \{w'\}^T[P_0]\{w'\}dS = \frac{1}{2}\lambda\iint_S \{w'\}^T[P_0]\{w'\}dS \tag{6}$$

and

$$\{w'\} = \begin{Bmatrix} \dfrac{\partial w}{\partial r} \\ \dfrac{1}{r}\dfrac{\partial w}{\partial \theta} \end{Bmatrix}, \qquad [P_0] = \begin{bmatrix} P_x & P_{xy} \\ P_{xy} & P_y \end{bmatrix} \tag{7}$$

$$[A] = \int_{-h/2}^{h/2} [C]\, dz$$

$$[B] = \int_{-h/2}^{h/2} [C]\, z dz \tag{8}$$

$$[D] = \int_{-h/2}^{h/2} [C]\, z^2 dz$$

$[P_0]$ is the applied load and [C] is the elastic stiffness matrix. $\{\ \}^T$ means the transpose of $\{\ \}$.

To obtain an approximate solution for the problem, we assume the in-plane displacements u and v, and the out-of-plane displacement w in the following series:

$$u = \sum_{i,j}^{N_i,N_j} \Phi_{u_{ij}}\, U_{ij}$$

$$v = \sum_{i,j}^{N_i,N_j} \Phi_{v_{ij}}\, V_{ij} \tag{9}$$

$$w = \sum_{ij}^{N_i,Nj} \Phi_{w_{ij}}\, W_{ij}$$

where $\Phi_{u_{ij}}, \Phi_{v_{ij}}, \Phi_{w_{ij}}$ are basis functions which depend on both r and θ coordinates. The coefficients U_{ij}, V_{ij}, and W_{ij} are unknown constants to be determined from the analysis. The basis functions for the displacements of a circular sublaminate are chosen as follows

$$\Phi_{u_{ij}} = [1 - \cos(\frac{(2i-1)\pi r}{2R})]\ F_j(r,\theta) \tag{10}$$

$$\Phi_{vij} = \sin(\frac{(2i-1)\pi r}{2R})\ F_j(r,\theta) \tag{11}$$

$$\Phi_{w_{ij}} = [\cos(\frac{i\pi r}{R}) + \cos(\frac{(i-1)\pi r}{R})]\ G_j(r,\theta) \tag{12}$$

with

$$F_j(r,\theta) = \begin{cases} 1\ , & j = 1 \\ r\cos j\theta, & j = 2k+1 \\ r\sin j\theta, & j = 2k \end{cases} \tag{13}$$

and

$$G_j(r,\theta) = \begin{cases} 1, & j = 1 \\ r^2\cos j\theta, & j = 2k+1 \\ r^2\sin j\theta, & j = 2k \end{cases} \tag{14}$$

where k = 1, 2, 3, ...

Note that the above assumed displacements satisfy all the clamped conditions along the boundary $r = R$, that is

$$u(0,\theta) = 0, \quad v(0,\theta) = 0, \quad v(R,\theta) = 0$$

$$w(R,\theta) = 0, \quad w_{,r}(0,\theta) = 0, \quad w_{,r}(R,\theta) = 0 \tag{15}$$

Substituting the assumed displacements in (9) into the potential energy expression in (3), we obtain an expression for π in terms of unknown displacements U_{ij}, V_{ij}, and W_{ij}. Taking the first variation of Π and letting $\delta\Pi = 0$, the following governing equation can be derived:

$$\begin{bmatrix} K_u & K_{uw} \\ K_{uw}^T & K_w \end{bmatrix}\begin{Bmatrix} U \\ W \end{Bmatrix} + \begin{bmatrix} 0 & K_{nuw} \\ K_{nuw}^T & K_{nw} \end{bmatrix}\begin{Bmatrix} U \\ W \end{Bmatrix} - \lambda\begin{bmatrix} 0 & 0 \\ 0 & K_G \end{bmatrix}\begin{Bmatrix} U \\ W \end{Bmatrix} = 0 \tag{16}$$

where the $\{U\}$ vector contains the coefficients U_{ij} and V_{ij} while the vector $\{W\}$ contains W_{ij}. All the stiffness matrix

terms in Eq. (16) such as $[K_u]$, $[K_{uw}]$, $[K_w]$, etc. can be calculated using the constitutive equation and geometric relations. They are:

$$[K_u]=[B_u]^T[A][B_u]\ , \qquad [K_{uw}]=[B_u]^T[A][B_w]$$

$$[K_w]=[B_w]^T[A][B_w]\ , \qquad [K_{nuw}]=[B_u]^T[A][B_n]$$

$$[K_{nw}]=[B_n]^T[A][B_n]+[B_w]^T[B][B_n]+[B_n]^T[B][B_w]$$

$$[K_G]=[B_G]^T[P_0][B_G] \tag{17}$$

where

$$[B_u]=\left[\frac{\partial\Phi_{ui}}{\partial r}\ ,\ 0\ ,\ \frac{1}{r}\Phi_{ui}\ ,\ \frac{1}{r}\frac{\partial\Phi_{vi}}{\partial\theta}\ ,\ \frac{1}{r}\frac{\partial\Phi_{ui}}{\partial\theta}\ ,\ \frac{\partial\Phi_{vi}}{\partial r}-\frac{1}{r}\Phi_{vi}\right]^T$$

$$[B_w]=\left[-\frac{\partial^2\Phi_{wk}}{\partial r^2}\ ,\ -\frac{1}{r^2}\frac{\partial^2\Phi_{wk}}{\partial\theta^2}-\frac{1}{r}\frac{\partial\Phi_{wk}}{\partial r}\ ,\ -\frac{2}{r}\frac{\partial^2\Phi_{wk}}{\partial r\partial\theta}+\frac{1}{r^2}\frac{\partial\Phi_{wk}}{\partial\theta}\right]^T$$

$$[B_n]=\left[\frac{1}{2}\frac{\partial\overline{w}}{\partial r}\frac{\partial\Phi_{wk}}{\partial r}\ ,\ \frac{1}{2r^2}\frac{\partial\overline{w}}{\partial\theta}\frac{\partial\Phi_{wk}}{\partial\theta}\ ,\ \frac{1}{2r}\left(\frac{\partial\overline{w}}{\partial r}\frac{\partial\Phi_{wk}}{\partial\theta}+\frac{\partial\overline{w}}{\partial\theta}\frac{\partial\Phi_{wk}}{\partial r}\right)\right]^T$$

$$[B_G]=\left[\frac{\partial\Phi_{wk}}{\partial r}\ ,\ \frac{1}{r}\frac{\partial\Phi_{wk}}{\partial\theta}\right]^T \tag{18}$$

By eliminating the {U} vector from Eq. (16), we obtain

$$[K_{wa}]\{W\}-\lambda[K_G]\{W\}=0 \tag{19}$$

The matrix $[K_{wa}]$ is a nonlinear term obtained from the matrices $[K_u]$, $[K_w]$ *etc* as :

$$[K_{wa}]=[K_w]+[K_{nw}]+[K_{ns}]-([K_{uw}]+[K_{nuw}])^T[K_u]^{-1}([K_{uw}]+[K_{nuw}]) \tag{20}$$

where

$$[K_{ns}]=\frac{1}{2}[B_G]^T[S][B_G]\ , \qquad [S]=\begin{bmatrix}S_x & S_{xy}\\ S_{xy} & S_y\end{bmatrix} \tag{21}$$

The components of [S] are given by:

$$\{S\}=[S_x,\ S_y,\ S_{xy}]^T=[A]\{\varepsilon_0\}+[A]\{\varepsilon_n\}+[B]\{\chi\} \tag{22}$$

An iterative procedure was employed to solve the above non-linear eigenvalue problem given in Eq. (19). The numerical procedure included the following steps:

1. Calculate the bifurcation buckling load and the corresponding buckling mode.
2. Assume an incremental deflection and use the stiffness matrix from the previous step to obtain the next post buckling load and displacement.
3. Use the Newton-Raphson method to modify the stiffness matrix and update the post buckling load.
4. Check the convergence of the solution. If the method has not converged, go to step 3. If converged, go to step 2.

The above formulation was used to determine the postbuckling behavior of an orthotropic layer at an angle θ from the loading direction. The material properties used in the analysis are: $E_1=17.57E_2$, $\nu_{12}=0.28$, $G_{12}=0.5E_2$. The plate is subjected to a uniform compressive strain of $\bar{\varepsilon}_x$ in the x direction and a tensile strain of $0.3\bar{\varepsilon}_x$ in the y directions. The biaxial strains were applied for comparison purposes. A convergence study was first conducted to determine the number of terms that was required in the series. It was found that the solution converged with $N_i=4$ and $N_j=8$ terms. Next, the post buckling solutions of circular sublaminates with $\theta=0°$, $30°$, and $45°$ were obtained. These results are plotted in Figure 2 in the form of normalized maximum deflection, w/h, versus the applied strain $\bar{\varepsilon}_x$. Note that the present solutions compare well with those obtained by Yin, et al [3] using a different set of basis functions.

Analysis of CAI Strength

Dost, Ilcewicz, and Gosse (DIG) proposed a method for predicting the CAI strength of composite laminates[1]. Their approach was based on the assumption that the compressive failure of a composite was triggered by the strain concentration near the damaged zone where the stiffness is reduced due to local buckling. The damaged zone was assumed to follow a linear load-deflection path until it was buckled. After buckling, loads carried by the sublaminate became a constant, as in the Euler buckling

case. The reduced stiffness of the buckled damage zone was calculated at failure point by ensuring a strain compatibility at the boundary between a damaged and an undamaged laminate, that is,

$$E^* = \frac{\varepsilon_{cr}}{\varepsilon_0} E \tag{23}$$

where E^* is the reduced stiffness and ε_{cr} is the critical buckling strain and ε_u is the failure strain of undamaged laminate.

Since the sublaminate can further carry loads after buckling occurs, the reduced stiffness is actually a function of the transverse deflection w. In order to accurately calculate the reduced stiffness, postbuckling solutions of a sublaminate must be obtained as was done in the previous section. Using these solutions, the reduced stiffness can be calculated as follows.

If the laminate has a linear load-deflection path, we have

$$U_l = k\frac{P}{E} \tag{24}$$

where U_l is the maximum inplane displacement, P is the axial load and k is a geometric parameter which is a constant.

In a nonlinear postbuckling solution, the maximum inplane displacement is

$$U_{nl} = k^* \frac{P}{E} \tag{25}$$

where k^* depends on P. If the geometric parameter k is considered to be a constant and the material parameter E is changing during postbuckling, the relation can be written as

$$U_{nl} = k\frac{P}{E^*} \tag{26}$$

Thus, the reduced stiffness E^* can be defined as

$$E^* = \frac{U_l}{U_{nl}} E \tag{27}$$

Eq. (27) has been used for calculating the reduced stiffness of $(45/0\text{-}45/90)_{3S}$ graphite/epoxy with a circular delamination. The results are shown in Figure 3 for different damage sizes and compared with those obtained by the DIG model.

After the reduced stiffness is obtained, the stress concentration factor K_t can be found using the finite element method by treating the sublaminate as a soft inclusion. The residual strength of the laminate, σ_r, is then calculated from

$$\sigma_r = \frac{\sigma_0}{K_t} \tag{28}$$

where σ_0 is the strength of undamaged laminates.

Experimental Verification

Experiments were conducted to gain further insight into the behavior of impact damaged composite panels under compressive loads. The test samples were made of IM7/8551 graphite/epoxy with a $(45/0/\text{-}45/90)_{3S}$ layup. The dimensions of specimen were 4 in. (10.16 cm) wide by 6 in. (15.24cm) long with a nominal thickness of 0.18 in. (0.457 cm) (24 plies). Each specimen was impacted with a Dynatup drop weight impactor to create a damaged zone in the center. After the specimens were impacted, the damage state of each specimen was analyzed using the ultrasonic C-scan. The effective damage radius of these specimens was found to be in the range of 0.328 in. to 0.642 in. (0.833 cm to 1.631 cm).

The impacted specimens were tested in static compression to determine local damage region behavior as well as the residual strength. In-plane displacements *(u,v)* on the impacted side were measured using a micro moire interferometry technique[4]. The grating used was a 4 in.(10.16 cm) by 4 in. reflective, phase type diffraction grating with a frequency of 600 lines/mm (15,240 lines/in) in both vertical and horizontal directions. This grating yielded a resolution for the displacement of $0.833\text{x}10^{-6}$m ($3.281\text{x}10^{-5}$in). Application of the grating required extensive specimen preparation. The impacted side was sanded until flat and relatively smooth. The grating was then mounted to the specimen using an epoxy adhesive. A small reference line was scored onto the grating to provide a length scale in the photographs of the fringes.

The out-of-plane displacement in the opposite side of the specimen was measured by employing shadow moire interferometry. The specimen surface was also sanded to achieve a smooth surface, but then spray-painted with a self-priming metallic silver paint. A reference cone with a height of 0.077 in. (0.196 cm) and a base diameter of 0.485 in. (1.232 cm) was then attached to one corner of the painted surface. Fringes were created by placing a 60 lines/cm (152 lines/in) glass mounted grating in front of this surface, and illuminating and then viewing the surface from specified angles.

Compression testing was accomplished by clamping the specimen into a fixture designed to stabilize it against

global buckling[5], and placing the fixture in a static test machine. An 8-mirror interferometry setup was used to generate fringe patterns for axial and transverse displacements in a circular region of approximately 3.25 in. (8.225 cm) in diameter. Light was directed from the 35 mW He-Ne laser into the spatial filter and aspherical lenses. The collimated light went through the interferometer set and produced fringe patterns on the specimen. The fringe pattern image was reflected by another mirror through a lense and into the camera. The measured u, v fringes were then scanned into a Macintosh II computer and differentiated into a strain field from which the strain concentration factors were obtained. Out-of-plane data were analyzed by viewing the negatives of photos taken by the camera with a microfiche projector. The height and base diameter of the reference cone were used as length scales for measuring buckling area diameter and maximum out-of-plane displacement. Details of the experimental setup and procedure can be found in [5].

Typical moire fringe patterns for axial (u) deformations in the loading direction at four different percentages of the failure load are shown in Figure 4. The resulting ε_x strain data are shown in Figure 5. Note that the magnitude and areas of strain concentration increase with applied loads. Numerical values for the strain concentration factors are plotted in Figure 6 and compared with those predicted from the soft-inclusion model. Since the severity of impact damage varies in the damaged region, a wide range of strain concentration was found. However, the predictions generally fall within the upper and lower bounds of the measured value.

The CAI strengths for specimens with different damage radius were also measured and were plotted in Figure 7. These data were compared with analytical predictions using the DIG model with critical buckling loads and the present postbuckling solutions. While both the DIG and the present solutions agree well with the experimental data, it appears that the present solution yields better predictions, particularly for a large damage diameter.

Conclusion

An analytical solution has been obtained for the postbuckling of composite laminates with a circular delamination. Using this solution, the reduced stiffness of the impacted region and the compression-after-impact strength have been determined as a function of effective damage diameter. The predicted strain fields and compressive strengths compare well with the experimental data. In addition, experimental results indicate that static compressive failure is triggered by the strain concentration of the damaged region rather than the growth of impact damage.

Acknowledgements

This work is supported by the Boeing company as a subcontract from the NASA Langley Research Center. The authors wish to thank Mr. E. F. Dost and L. B. Ilcewicz of the Boeing Co. for their valuable discussions, and Mr. J. J. Stevens and X. J. Zhang of the University of Washington for their assistance in the experiment.

References

1. Dost, E. F., Ilcewicz, L. B., and Gosse, J. H., "Sublaminate Stability Based Modeling of Impact Damage Composite Laminates," Proc. of the 3rd Technical Conf., American Society for Composites, 1988, p. 354.
2. Shivakumar, K. N. and Whitcomb, J. D., "Buckling of a Sublaminate in a Quasi-Isotropic Composite Laminate," J. of Composite Materials, Vol. 19, Jan. 1985, p.2.
3. Yin, W.-L., and Jane, K. C. "Refined Buckling and Postbuckling Analysis of Two-Dimensional Delaminations" Int. J. Solids & Structures, Vol. 29, No. 5, 1992, p. 591.
4. Post, D., "Moiré Interferometry," Handbook on Experimental Mechanics, Edited by A. S. Kobayashi, Prentice Hall, 1987.
5. Lin, K. Y. and Stevens, J. J. "Characterization of Post Impact Compressive Behavior of Composite Laminates", Interim Report, The Boeing Co., Contract NAS1-18889, June 1992.

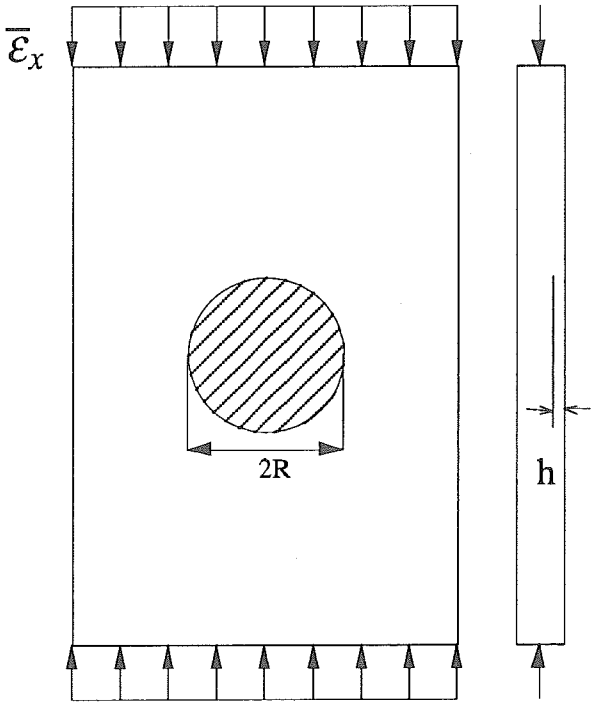

Fig.1 Geometry of a Delamination

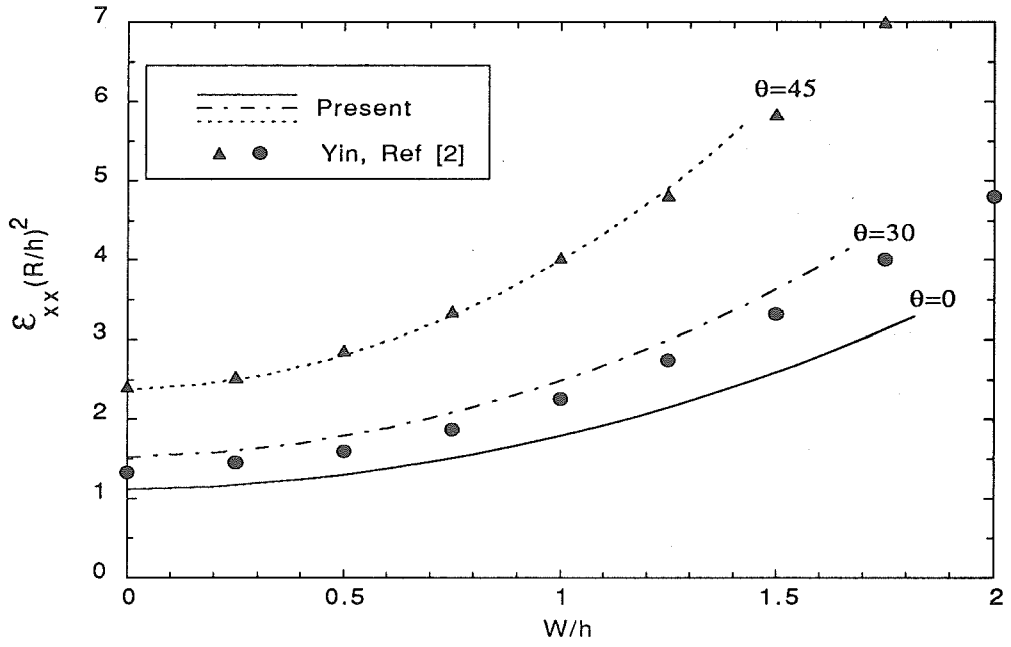

Fig. 2 Post Buckling Solution for Circular Delaminations

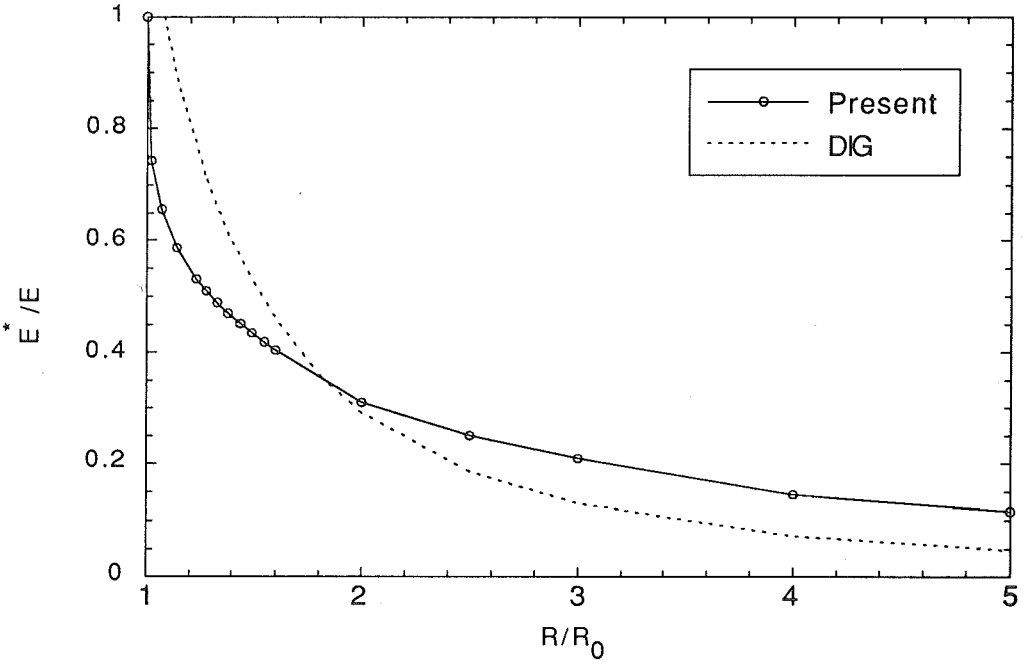

Fig.3 Residual Stiffness versus Damage Radius

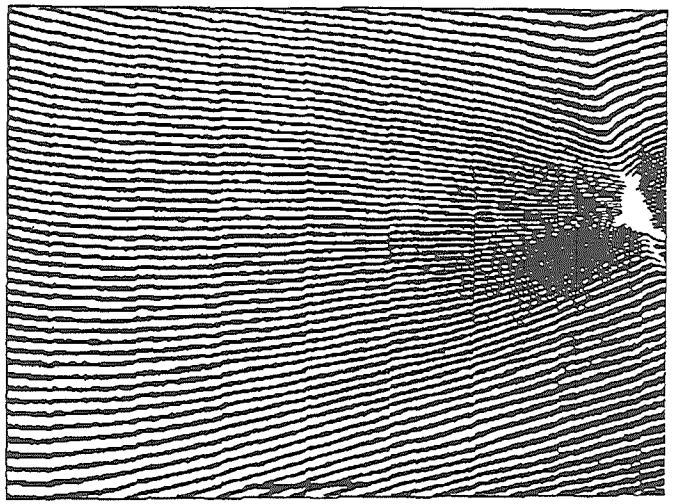

At 55% of Failure Load (10,000 lb)

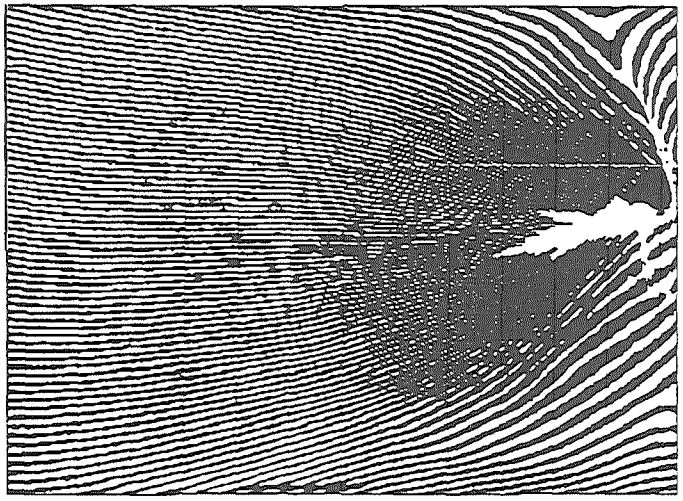

At 70% of Failure Load (13,000 lb)

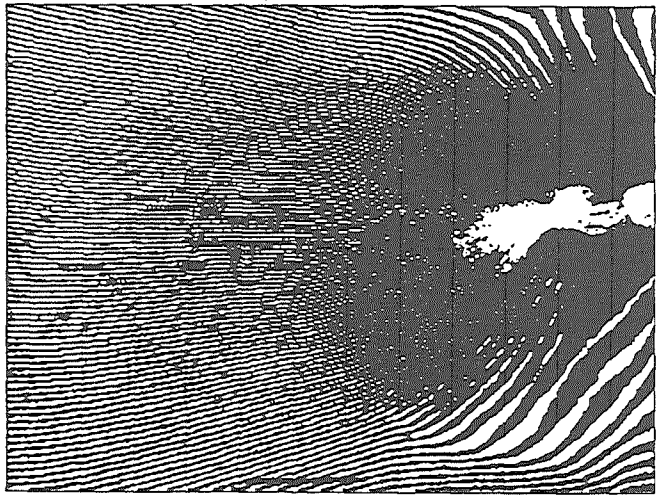

At 83% of Failure Load (15,500 lb)

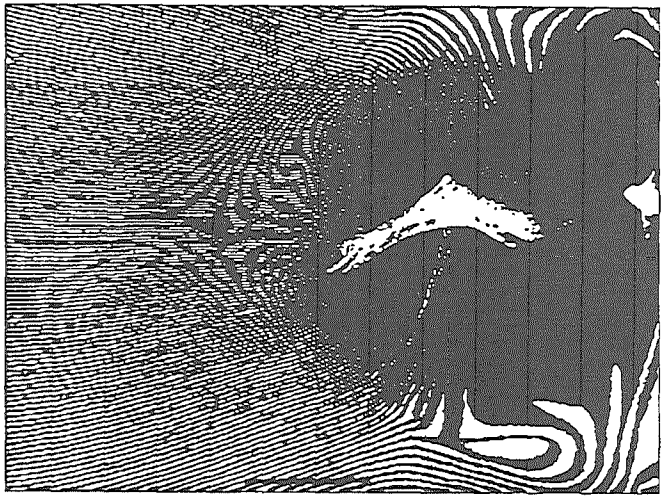

At 98% of Failure Load (18,200 lb)

Fig. 4 Axial Displacement Fringes vs. Applied Loads

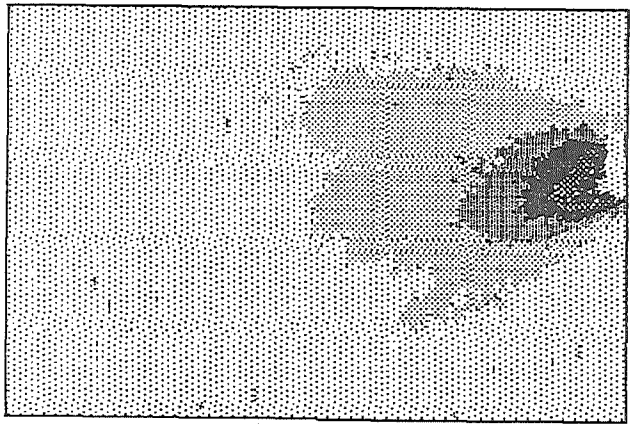

At 55% of Failure Load (10,000 lb)

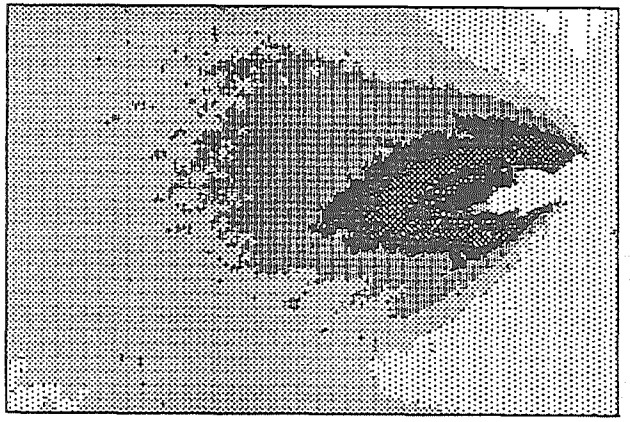

At 70% of Failure Load (13,000 lb)

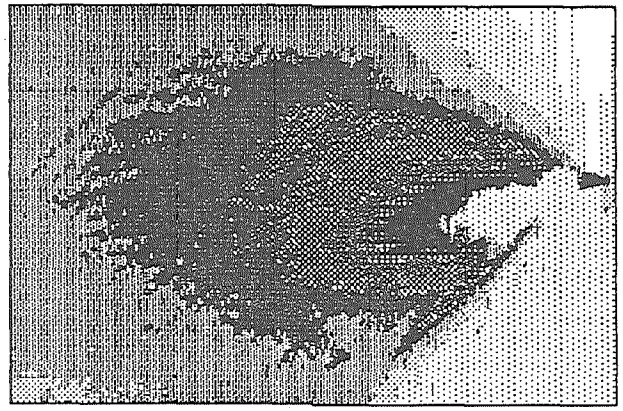

At 83% of Failure Load (15,500 lb)

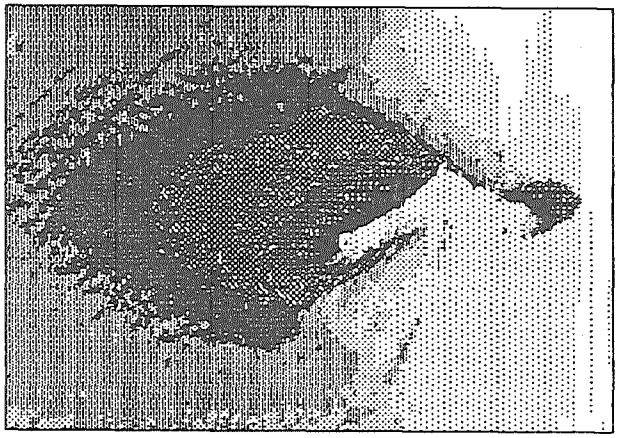

At 98% of Failure Load (18,200 lb)

Fig. 5 Axial Strain Fields vs. Applied Loads

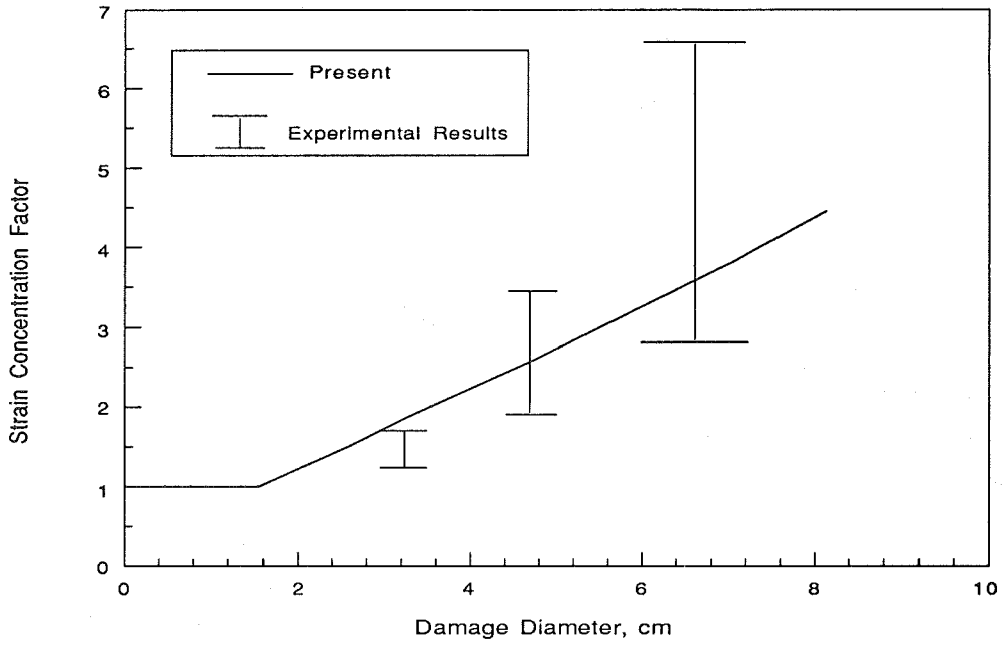

Fig. 6 Strain Concentration Factor vs. Damage Diameter

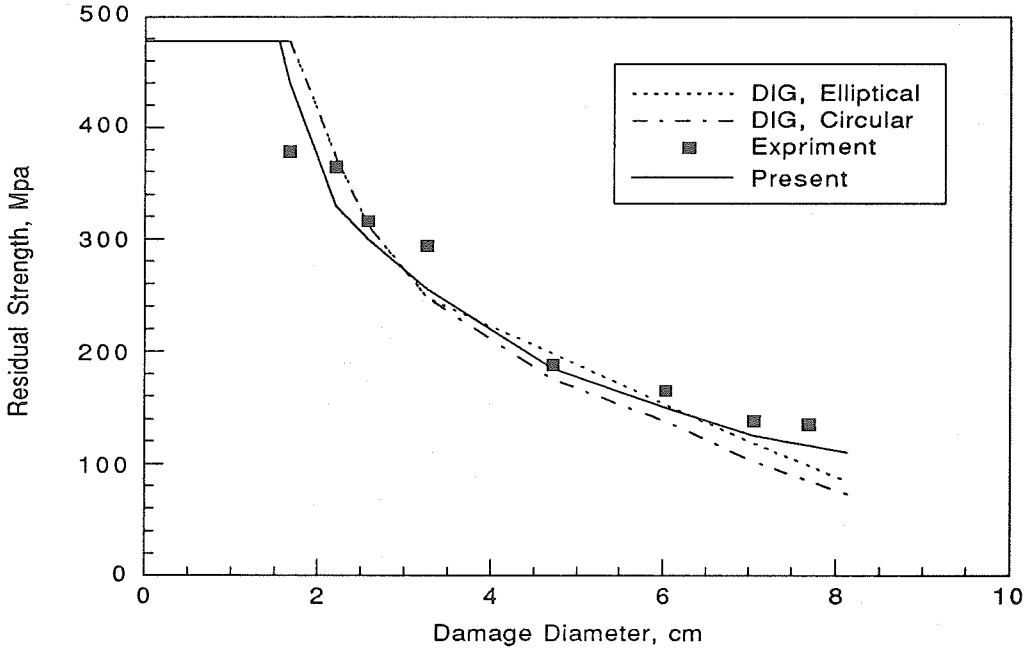

Fig. 7 Comparison of Predicted Residual Strength with Experimental Data